

This is the accepted manuscript made available via CHORUS. The article has been published as:

Superconducting state in the metastable binary bismuthide $\text{Rh}_{\{3\}}\text{Bi}_{\{14\}}$ single crystals

Xiao Zhang (张肖), Hechang Lei (李恒昌), and C. Petrovic

Phys. Rev. B **86**, 054502 — Published 1 August 2012

DOI: [10.1103/PhysRevB.86.054502](https://doi.org/10.1103/PhysRevB.86.054502)

Superconducting state in the metastable binary bismuthide $\text{Rh}_3\text{Bi}_{14}$ single crystals

Xiao Zhang(张晓), Hechang Lei (雷和畅) and C. Petrovic
Condensed Matter Physics and Materials Science Department,
Brookhaven National Laboratory, Upton, NY 11973, USA
(Dated: July 16, 2012)

We report detailed magnetic, transport and thermodynamic properties of metastable $\text{Rh}_3\text{Bi}_{14}$ single crystals in superconducting and normal state. We show that $\text{Rh}_3\text{Bi}_{14}$ is nearly isotropic, weak to intermediately coupled BCS superconductor, whereas the electronic resistivity above superconducting $T_c = 2.94$ K is dominated by the phonon scattering in the large unit cell with pores filled by Bi atoms. Superconductivity is strongly influenced by the nature of atoms that fill the voids in the crystal structure.

PACS numbers: 74.25.-q, 74.70.Ad, 74.62.Bf

I. INTRODUCTION

Complex crystal structures with atomic subunits often show significant electronic and magnetic tunability through incorporation of various elements in the (sub)structure. Examples include covalently bonded IV group thermoelectric clathrates that are under influence of anharmonic lattice vibrations with electron - phonon coupling strength comparable to MgB_2 , alkali doped fullerenes and magnetic molecules.¹⁻⁸ Cluster units may substantially define physical properties whereas their size may considerably deviate from the length scales defined by the lattice parameters, even in intermetallic systems where delocalized metallic bonds are present.⁹

Binary Rh-Bi intermetallic phase diagram has been studied for more than eight decades. Yet, structurally complex metastable $\text{Rh}_3\text{Bi}_{14}$ with 136 atoms per unit cell has been discovered only in the recent years.¹⁰⁻¹² Bismuth-rich side of this phase diagram includes also α - RhBi_2 , β - RhBi_2 , RhBi_3 and RhBi_4 phases.^{13,14} According to the Rh-Bi phase diagram, $\text{Rh}_3\text{Bi}_{14}$ is a metastable phase hidden in the RhBi_4 -Bi solid phase region. Since the kinetic of peritectic reaction forming RhBi_4 is extremely slow, it can be easily suppressed by undercooling due to nucleation problems.¹¹ Hence, $\text{Rh}_3\text{Bi}_{14}$ single crystals can be decanted from the Bi liquid whereas the RhBi_4 single crystals are difficult to obtain.

$\text{Rh}_3\text{Bi}_{14}$ has orthorhombic symmetry (Fddd space group) with $a = 0.69041(4)$ [0.68959(15)] nm, $b = 1.73816(9)$ [1.7379(3)] nm, and $c = 3.1752(2)$ [3.1758(6)] nm.^{11,12} In a $\text{Rh}_3\text{Bi}_{14}$ unit cell, there are 24 Rh and 112 Bi atoms.¹² Each Rh atom is surrounded by eight Bi atoms, however there are two inequivalent Rh positions in the unit cell. Rh1 is cubically coordinated, whereas Rh2 exhibits a square antiprismatic coordination as shown in Fig. 1(a). Each $[\text{RhBi}_8/2]$ polyhedra shares common edge with four other polyhedra, and thus create a porous three-dimensional (3D) framework with channels along the [100] direction. In these channels, there are chiral inner surfaces and filled with bismuth ions (Fig. 1(b)). Partial oxidation of RhBi_4 using bromine results in $\text{Rh}_3\text{Bi}_{12}\text{Br}_2$, isostructural with $\text{Rh}_3\text{Bi}_{14}$.¹² The difference between $\text{Rh}_3\text{Bi}_{14}$ and $\text{Rh}_3\text{Bi}_{12}\text{Br}_2$ is in the atoms

in the channels. In $\text{Rh}_3\text{Bi}_{14}$, Bi atoms fill the channels, whereas they are filled by Br atoms in $\text{Rh}_3\text{Bi}_{12}\text{Br}_2$. The theoretical calculation indicates that the 3D polyhedral frameworks in $\text{Rh}_3\text{Bi}_{14}$ and $\text{Rh}_3\text{Bi}_{12}\text{Br}_2$ are formed by covalently bonded rhodium and bismuth atoms, consistent with the results of high pressure studies.¹² On the other hand, there are no direct bonds between this 3D polycation framework and anions (Bi^{-1} or Br^{-1} in the channels), which leads to the higher compressibility along a axis when compared to those along b and c axes mainly controlled by the covalently bonded polycation.¹²

Magnetization measurement indicates that $\text{Rh}_3\text{Bi}_{14}$ is a superconductor with $T_c = 2.82(5)$ K.¹¹ Although the crystal structure and chemical bonding have been studied,^{11,12,15} the studies on physical properties, especially in connection with superconductivity are still lacking.¹¹ In this work, we report detailed analysis of $\text{Rh}_3\text{Bi}_{14}$ physical properties in the superconducting and normal states. We show that electronic scattering in the normal state is dominated by phonons, whereas in its superconducting state $\text{Rh}_3\text{Bi}_{14}$ is an isotropic, weakly to intermediately coupled BCS superconductor.

II. EXPERIMENTAL

Single crystals of $\text{Rh}_3\text{Bi}_{14}$ were grown by the flux-growth method with Rh:Bi = 5:95 molar ratio. Rh pieces (99.9 %) and Bi shot (99.9 %) were weighed, combined into alumina crucible, covered with quartz wool and sealed into the quartz tube with partial pressure of argon. The quartz tube was heated to 1000 °C held constant for 2 h and then cooled at a rate of -3.5 °C/h to 300 °C where crystals were decanted. Single crystals with typical size $0.5 \times 0.2 \times 0.2$ mm³ were obtained. Crystal structure and phase purity were examined by powder and single crystal X-ray diffraction pattern (XRD) with Cu K_α radiation ($\lambda = 0.15418$ nm) using a Rigaku Miniflex X-ray machine. The structure parameters are extracted by fitting the XRD spectra using the Rietica software.¹⁶ Crystal was oriented using Bruker SMART APEX II single crystal X-ray diffractometer. The composition of $\text{Rh}_3\text{Bi}_{14}$ single crystal was determined by examination of multi-

FIG. 1. (a) Crystal structure of $\text{Rh}_3\text{Bi}_{14}$. Three-dimensional framework is built of $[\text{RhBi}_{8/2}]$ cubes and square antiprisms which share common edges. Bi4 atoms fill the channels of the framework. (b) Edge-sharing $[\text{RhBi}_{8/2}]$ cubes and square antiprisms enclosing bismuth ions form the zigzag channel in $\text{Rh}_3\text{Bi}_{14}$. (c) Powder XRD pattern of $\text{Rh}_3\text{Bi}_{14}$ single crystal. (d) The EDX spectrum of a single crystal.

FIG. 2. (a) Temperature dependence of the resistivity $\rho_a(T)$ of $\text{Rh}_3\text{Bi}_{14}$. Inset: resistivity near T_c . (b) Temperature dependence of dc magnetic susceptibility of $\text{Rh}_3\text{Bi}_{14}$ with ZFC and FC at 10 Oe for $H \parallel a$, $H \parallel b$ and $H \parallel c$. The superconducting transition temperature $T_{c,onset}$ are marked by arrow.

ple points on the crystals using energy dispersive X-ray spectroscopy (EDX) in an JEOL JSM-6500 scanning electron microscope. Electrical transport, heat capacity, and magnetization measurements were performed in a Quantum Design PPMS-9 and MPMS XL 5.

III. RESULTS AND DISCUSSION

All powder X-ray reflections (Fig. 1(c)) can be indexed in the $Fddd$ space group. The refined lattice parameters are $a = 0.6891(1)$ nm, $b = 1.7388(1)$ nm, $c = 3.1718(2)$ nm with $R_p = 5.220$, $R_{wp} = 6.720$ and $\chi^2 = 0.919$, consistent with the values reported in literature.^{11,12} On the other hand, we also refined the lattice parameters using single crystal XRD. The lattice parameters are $a = 0.707(3)$ nm, $b = 1.755(5)$ nm and $c = 3.154(8)$ nm, which are also close to the result obtained from powder XRD and previous results. EDX spectrum of a single crystal (Fig. 1(d)) confirms the presence of only Rh and Bi with the average atomic ratios Rh:Bi = 3.0(4):13.8(4).

The temperature dependent electrical resistivity $\rho(T)$ of $\text{Rh}_3\text{Bi}_{14}$ is shown in Fig. 2(a). The sharp resistivity drop with $T_{c,onset} = 3.04$ K is caused by superconducting transition (inset of Fig. 2(a)). The residual resistivity ratio (RRR), defined as $\rho(295\text{K})/\rho(3.04\text{K})$, is about 9.3. The curve $\rho(T)$ is convex above 50 K, with a tendency to saturate at high temperature. The saturation of $\rho(T)$ could be related to the Ioffe-Regel limit,¹⁷ when the charge carrier mean free path is comparable to the interatomic spacing and/or to the two-band conductivity.¹⁸ According to the phenomenological model:¹⁹

$$\frac{1}{\rho(T)} = \frac{1}{\rho_{ideal}} + \frac{1}{\rho_{sat}}, \text{ with } \rho_{sat} \approx \frac{v_F}{\varepsilon_0 \Omega_p^2 a} \quad (1)$$

where v_F is the Fermi velocity, Ω_p is the plasma frequency, a is interatomic spacing and $\rho_{ideal} = \rho_r + \rho_i(T)$. The $\rho_i(T)$ is the inelastic resistivity due to the phonon contribution whereas ρ_{sat} is the saturation resistivity. Phonon contribution can be explained by the Bloch-

FIG. 3. (a) Magnetization hysteresis loops of $\text{Rh}_3\text{Bi}_{14}$ at $T = 1.8$ K for $H \parallel a$, $H \parallel b$ and $H \parallel c$. (b), (c) and (d) Low field parts of $M(H)$ at various temperature for $H \parallel a$, $H \parallel b$ and $H \parallel c$ with demagnetization correct, respectively. The solid blue lines are the “Meissner line” as discussed in the text. (e) Temperature dependence of H_{c1} for $H \parallel a$, $H \parallel b$ and $H \parallel c$. The dashed lines are the fitted lines using $H_{c1} = H_{c1}(0)(1 - (T/T_c)^2)$. (f) the temperature dependence of anisotropy of H_{c1} , $\gamma_{H_{c1}} = H_{c1,a}(T)/H_{c1,b}(T)$, $\gamma_{H_{c1}} = H_{c1,c}(T)/H_{c1,b}(T)$, $\gamma_{H_{c1}} = H_{c1,c}(T)/H_{c1,a}(T)$.

Grüneisen formula:

$$\rho_i(T) = \left(\frac{c}{\Theta_D}\right) \left(\frac{T}{\Theta_D}\right)^5 \int_0^{\Theta_D/T} \frac{x^5}{(e^x - 1)(1 - e^{-x})} dx \quad (2)$$

where Θ_D is the Debye temperature, c is a constant which depends on the electronic structure of the metal through the Fermi velocity v_F and the density of states at the Fermi energy.²⁰ The fitting result over the full temperature range of ρ_T is shown in Fig. 2(a) as a solid line, revealing an excellent agreement between the model and data for $\rho_r = 60.0(4) \mu\Omega\cdot\text{cm}$, $\rho_{sat} = 640(2) \mu\Omega\cdot\text{cm}$, $\Theta_D = 95.0(8)$ K, $c = 27.7(6) \times 10^4 \mu\Omega\cdot\text{cm}$.

To confirm the presence of bulk superconductivity in $\text{Rh}_3\text{Bi}_{14}$ single crystals, the magnetization is measured using dc susceptibility method. Fig. 2(b) shows the temperature dependence of the dc susceptibility for a crystal with dimension of $0.2 \times 0.4 \times 0.2 \text{ mm}^3$ for $H \parallel a$, $H \parallel b$ and $H \parallel c$ with zero-field cooling (ZFC) and field cooling (FC) under an applied magnetic field of 10 Oe. The steep transition show that the $\text{Rh}_3\text{Bi}_{14}$ single crystal has a superconducting transition temperature for all field directions of 2.91 K ($T_{c,onset}$) with a transition width $\Delta T_c = 0.30$ K, consistent with the result of resistivity measurement. At 2 K, the ZFC dc susceptibility approaches a value of -1 for all directions after demagnetization correction, indicating bulk superconductivity. The FC signal shows a flux exclusion of 61 %, 70 % and 81 % for $H \parallel a$, $H \parallel b$ and $H \parallel c$ respectively. The big superconducting volume fraction for FC indicates the rather weak flux pinning effects.

The shape of $M(H)$ curve at 1.8 K (Fig. 3(a)) confirms weak pinning, in agreement with Fig. 2(b). In order to obtain the lower critical fields of $\text{Rh}_3\text{Bi}_{14}$, we measured the initial $M(H)$ curves at various temperatures with the field directions along the a -, b - and c -axis. For each field direction, all curves clearly fall on the same line and deviate from linearity for different temperature. Linear fits for the initial parts of magnetization curves describe the Meissner shielding effects (“Meissner line”).

The value of H_{c1}^* at which the field starts to penetrate into the sample can be determined by examining the point of deviation from the Meissner line on the initial slope of the magnetization curve. The first penetration field H_{c1}^* is not the same as the real lower critical field H_{c1} , due to the geometric effect. The H_{c1} can be deduced from the H_{c1}^* , assuming that the magneti-

FIG. 4. (a) Temperature dependence of the resistivity in a set of magnetic fields from 0 to 6 kOe for (a) $H \parallel b$ and (b) $H \parallel c$. (c) Temperature dependence of the upper critical field H_{c2} for $H \parallel b$ and (b) $H \parallel c$.

ization $M = -H_{c1}$ when the first vortex enters into the sample. Thus H has been rescaled to $H = H_a - NM$ and $H_{c1} = H_{c1}^*/(1 - N)$ where N is the demagnetization factor and H_a is the external field.²¹ We estimate demagnetization factors 0.47, 0.23 and 0.59 for $H \parallel a$, $H \parallel b$ and $H \parallel c$ by using $H_{c1} = H_{c1}^*/\tanh(\sqrt{0.36b/a})$, where a and b are width and thickness of a plate-like superconductor.²² The corrected data are plotted in Fig. 3(b), (c) and (d). Considering the demagnetization factors, the obtained slopes of the linear fitting at the lowest temperature of our measurements $T = 1.8$ K are -0.972(2), -0.988(2) and -0.987(2), very close to -1 ($4\pi M = -H$) for all field directions. Thus the full Meissner shielding effect in our measurement provides a reliable way to determine the value of H_{c1} .

H_{c1} is determined as the point deviating from linearity based on the criterion $\Delta M = (M_m - M_{th}) = 2 \times 10^{-6}$ emu, M_m is the measured moment value and M_{th} is fitted moment value at the same external field. From Fig. 3(b), (c) and (d), H_{c1}^a , H_{c1}^b and H_{c1}^c values at the different temperatures can be obtained as shown in Fig. 3(e). The $H_{c1}(T)$ can be fitted according to $H_{c1}(T) = H_{c1}(0)[1 - (T/T_c)^2]$. Fitting lines are shown in Fig. 3(e). The obtained $H_{c1}^a(0)$, $H_{c1}^b(0)$ and $H_{c1}^c(0)$ are 90(1), 63(1) and 93(1) Oe respectively. The anisotropy of H_{c1} along each axis can be determined as shown in Fig. 3(f). It can be seen that the anisotropy of $H_{c1}(T)$ is very close to 1, especially for $H \parallel c$ and $H \parallel a$, indicating that $\text{Rh}_3\text{Bi}_{14}$ is a nearly isotropic superconductor.

With increasing magnetic fields (Fig. 4(a) and (b)) the superconducting transition width broadens and the onsets of transition shift to lower temperatures gradually for both $H \parallel b$ and $H \parallel c$. When $H = 6$ kOe, the superconducting transition cannot be observed above 1.9 K for both field directions. It is interesting to observe kinks in the $R(T)$ curves below T_c under fields for both field directions. The kinks are becoming more pronounced with the increasing field. The origin of these kinks implies rich vortex physics, similar to NbSe_2 .²³ The upper critical field H_{c2} is determined by the criterion of 90 % of the normal state resistivity at various fields for both field directions (Fig. 4(c)). The slopes dH_{c2}/dT for $H \parallel b$ and $H \parallel c$ are equal to -6.47(5) kOe/K and -6.01(11) kOe/K, respectively. For dirty limit superconductors, $H_{c2}(0)$ can be obtained from the Werthammer-Helfand-Hohenberg formula:²⁴

$$H_{c2}(0) = -0.693 \frac{dH_{c2}}{dT} \big|_{T_c} T_c \quad (3)$$

yielding $H_{c2}^b(0) = 13.4(1)$ kOe and $H_{c2}^c(0) = 12.4(2)$ kOe. Since the Pauli limiting field $H_p(0) = 18.4T_c \sim 52$ kOe,²⁵ the orbital effect should be the dominant pair-breaking

FIG. 5. (a) Low temperature specific heat C_p/T vs. T^2 from 1.95 K to 300 K at $H = 0$ kOe. The solid line shows the fit (see text)(b) Temperature dependence of the electronic specific heat of $\text{Rh}_3\text{Bi}_{14}$ plotted as C_{es}/T vs T at $H = 0$ kOe.

mechanism. The small difference in the H_{c2} values for both field directions indicates that $\text{Rh}_3\text{Bi}_{14}$ shows almost isotropic $H_{c2}(T)$ as seen in Fig. 4(c).

Since $H_{c1}^a \approx H_{c1}^c$, according to the anisotropic Ginzburg-Landau (GL) theory, we assume $\xi_a \sim \xi_c$ and coherence length $\xi(0)$ can be estimated from the $H_{c2}(0)$ with: $H_{c2}^b(0) = \Phi_0/[2\pi\xi_a(0)\xi_c(0)]$ and $H_{c2}^c(0) = \Phi_0/[2\pi\xi_a(0)\xi_b(0)]$, where $\Phi_0 = 2.07 \times 10^{-15}$ Wb. Based on the values of $H_{c1}(0)$ and $H_{c2}(0)$, GL parameters $\kappa_i(0)$ is obtained from the equation $H_{c2}^i(0)/H_{c1}^i(0) = 2\kappa_i^2(0)/\ln \kappa_i(0)$, where i denotes the field applied along i direction. The thermodynamic critical field $H_c(0)$ can be obtained from $H_c(0) = H_{c2}^i(0)/[\sqrt{2}\kappa_i(0)]$. The GL penetration lengths are evaluated by the equations $\kappa_b(0) = \lambda_a(0)/\xi_c(0)$ and $\kappa_a(0) \approx \kappa_c(0) = \lambda_a(0)/\xi_b(0) = [\lambda_a(0)\lambda_b(0)/\xi_c(0)\xi_b(0)]^{1/2}$. The anisotropy is $\gamma_{anis} = H_{c2}^b(0)/H_{c2}^c(0) = \xi_b(0)/\xi_c(0)$.²⁶ All of the obtained parameters are listed in Table 1.

Specific heat divided by temperature (Fig. 5(a)) shows a jump at 2.94 K, indicating the bulk superconducting transition. Specific heat includes both the electron and lattice parts $C(T) = C_e(T) + C_{ph}(T)$. In the normal state, the specific heat of the lattice part is expressed by the βT^3 term at temperatures far below the Debye temperature Θ_D and electronic specific heat is assumed to be $\sim \gamma T$. Using $C_p/T = \gamma + \beta T^2$ we obtain (Fig. 5(a)) $\gamma = 8(1) \text{ mJ mol}^{-1} \text{ K}^{-2}$ and $\Theta_D \sim 113.9(7)$ K using $\Theta_D = (12\pi^4 N R / 5\beta)^{1/3}$, where $N = 17$ is the number of atoms per formula unit and R is the gas constant. Θ_D is similar to the value obtained from $\rho(T)$. The electron-phonon coupling constant λ_{e-ph} is obtained from the McMillan equation:

$$\lambda_{e-ph} = \frac{\mu^* \ln(1.45T_c/\Theta_D) - 1.04}{1.04 + \ln(1.45T_c/\Theta_D)(1 - 0.62\mu^*)} \quad (4)$$

and assuming the common value for the Coulomb pseudopotential $\mu^* \approx 0.13$. The value of λ_{e-ph} is determined to be 0.74(1) by using $T_c = 2.94$ K and $\Theta_D = 113.9(7)$ K. The value of λ_{e-ph} implies intermediately or weakly coupled BCS superconductivity. The electronic specific heat C_{es} in the superconducting state (Fig. 5(b)) is obtained by subtracting the lattice contribution estimated from the total specific heat. The extracted specific heat jump at $T_c(\Delta C/\gamma T_c = 1.8(2))$ is somewhat larger than the weak coupling value 1.43, and also points to intermediate coupling strength.²⁷

$\text{Rh}_3\text{Bi}_{12}\text{Br}_2$ has similar structure to $\text{Rh}_3\text{Bi}_{14}$, but the two Bi4 atoms are replaced by the Br atoms. $\text{Rh}_3\text{Bi}_{12}\text{Br}_2$ is a metal above 2 K without superconducting transition.¹⁵ From theoretical calculation,¹² the density of state (DOS) at Fermi energy is similar for both

TABLE I. Superconducting parameters of $\text{Rh}_3\text{Bi}_{14}$.

| $\text{Rh}_3\text{Bi}_{14}$ | T_c | H_{c1}^i | $H_{c2}^i(0)$ | $H_c^i(0)$ | $\kappa_i(0)$ | $\xi_i(0)$ | $\lambda_i(0)$ | γ_{anis} | γ_n | β | λ_{e-ph} | Θ_D | $\Delta C/\gamma_n T_c$ |
|-----------------------------|-------|------------|---------------|------------|---------------|------------|----------------|-----------------|--------------------------|--------------------------|------------------|------------|-------------------------|
| | (K) | (Oe) | (kOe) | (kOe) | | (nm) | (nm) | | (mJ/mol K ²) | (mJ/mol K ⁴) | | | |
| $i = a$ | 2.94 | 90(1) | | | | | 273(4) | 1.08(3) | 8(1) | 22.39(4) | 0.74(1) | 113.9(7) | 1.8(2) |
| $i = b$ | | 63(1) | 13.4(1) | 5.4(1) | 17.4(2) | 16.9(2) | 166(8) | | | | | | |
| $i = c$ | | 93(1) | 12.4(2) | 6.7(1) | 13.1(2) | 15.71(6) | | | | | | | |

compounds, however the contributions of atoms (s and p states of Bi) at Bi4 position to DOS are nearly removed when voids in the crystal structure are filled with Br atoms. Therefore, the superconductivity in $\text{Rh}_3\text{Bi}_{14}$ might be related to the s and p states of Bi atom in the interstitial Bi4 position of $\text{Rh}_3\text{Bi}_{14}$.

IV. CONCLUSION

In summary, we present a comprehensive study of the normal and superconducting state properties of metastable intermetallic superconductor, $\text{Rh}_3\text{Bi}_{14}$. The temperature dependence of resistivity $\rho(T)$ above the superconducting transition can be explained by the phonon

scattering. $\text{Rh}_3\text{Bi}_{14}$ is an isotropic, weakly to intermediately coupled BCS superconductor. Presence (absence) of superconductivity in $\text{Rh}_3\text{Bi}_{14}$ ($\text{Rh}_3\text{Bi}_{12}\text{Br}_2$) suggests that the nature of atoms that fill the pores in the structure is rather important.

V. ACKNOWLEDGMENTS

We thank Kefeng Wang for useful discussions and John Warren for help with SEM measurements. This work was performed at Brookhaven National Laboratory and supported by the US DOE under Contract No. DE-AC02-98CH10886.

-
- ¹ V. Crespi, *Nature Mater.* **2**, 651 (2003).
 - ² G.S. Nolas, J. L. Cohn, G.A. Slack, and S. B. Schujman, *App. Phys. Lett.* **73**, 178 (1998).
 - ³ N. P. Blake, L. Mollnitz, G. Kresse, and H. Metiu, *J. Chem. Phys.* **111**, 3133 (1999).
 - ⁴ T. Yokoya, A. Fukushima, T. Kiss, K. Kobayashi, S. Shin, K. Moriguchi, A. Shintani, H. Fukuoka, and S. Yamanaka, *Phys. Rev. B* **64**, 172504 (2001).
 - ⁵ J. D. Bryan, V. I. Srdanov, G. D. Stucky, and D. Schmidt, *Phys. Rev. B* **60**, 3064 (1999).
 - ⁶ F. M. Grosche, H. Q. Yuan, W. Carrillo-Cabrera, S. Paschen, C. Langhammer, F. Kromer, G. Sparrn, M. Baenitz, Y. Grin, and F. Steglich, *Phys. Rev. Lett.* **87**, 247003 (2001).
 - ⁷ B. C. Sales, B. C. Chakoumakos, R. Jin, J. R. Thompson, and D. Mandrus, *Phys. Rev. B* **63**, 245113 (2001).
 - ⁸ A. Muller, P. Kogerler, and C. Kuhlmann, *Chem. Comm.* **15**, 1347 (1999).
 - ⁹ K. Urban and M. Feuerbacher, *J. Non-Cryst. Solids* **334-335**, 143 (2004).
 - ¹⁰ E. J. Rode, *Izvest. Inst. Platiny Drug. Blagorodn. Met.* **7**, 21 (1929).
 - ¹¹ F. Weitzer, W. Schnelle, R. C. Gil, S. Hoffmann, R. Giedigkeit, and Y. Grin, *Computer Coupling of Phase Diagrams and Thermochemistry* **33**, 27 (2009).
 - ¹² Q. F. Gu, G. Krauss, Y. Grin, and W. Steurer, *J. Solid State Chem.* **180**, 940 (2007).
 - ¹³ A. Kjekshus, *Acta. Chem. Scand.* **25**, 41 (1971).
 - ¹⁴ M. Ruck, *Acta Crystallogr.* **B52**, 605 (1996).
 - ¹⁵ M. Ruck, *Solid State Sci.* **3**, 369 (2001).
 - ¹⁶ B. Hunter, *Comm. Powder Diffraction Newslett.*, **20**, 21 (1998).
 - ¹⁷ A. F. Ioffe and A. R. Regel, *Prog. Semicond.* **4**, 237 (1960).
 - ¹⁸ V. N. Zverev, A. V. Korobenko, G. L. Sun, D. L. Sun, C. T. Lin, and A. V. Boris, *JETP Lett.* **90**, 130 (2009).
 - ¹⁹ H. Wiesmann, M. Gurvitch, H. Lutz, A. Ghosh, B. Schwarz, M. Strongin, P. B. Allen, and J. W. Halley, *Phys. Rev. Lett.* **38**, 782 (1977).
 - ²⁰ Y. Fujimori, S. Kan, B. Shinozaki, and T. Kawaguti, *J. Phys. Soc. Jpn.* **69**, 3017 (2000).
 - ²¹ K. Fossheim and A. Sudbo, *Superconductivity: Physics and Applications* (John Wiley and Sons, West Sussex) (2004).
 - ²² E. H. Brandt, *Phys. Rev. B* **60**, 11939 (1999).
 - ²³ S. Bhattacharya and M. J. Higgins, *Phys. Rev. B* **49**, 10005 (1994).
 - ²⁴ N. R. Werthamer, E. Helfand, and P. C. Hohenberg, *Phys. Rev.* **147**, 295 (1966).
 - ²⁵ A. M. Clogston, *Phys. Rev. Lett.* **9**, 266 (1962).
 - ²⁶ J. R. Clem, *Physica (Amsterdam)* **162C-164C**, 1137 (1989).
 - ²⁷ W. L. McMillan, *Phys. Rev.* **167**, 331 (1968).

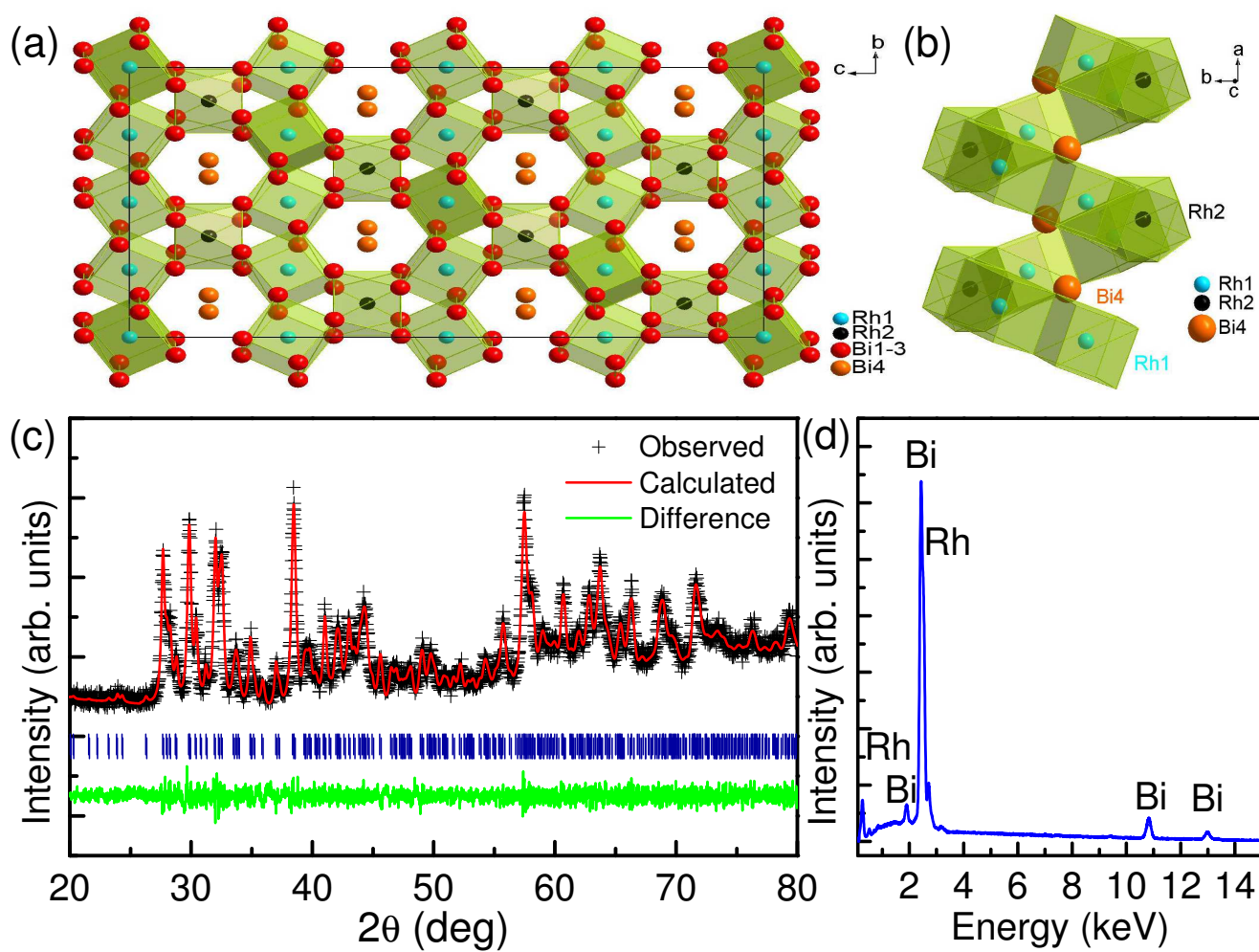


Figure 1 BR11786 16Jul2012

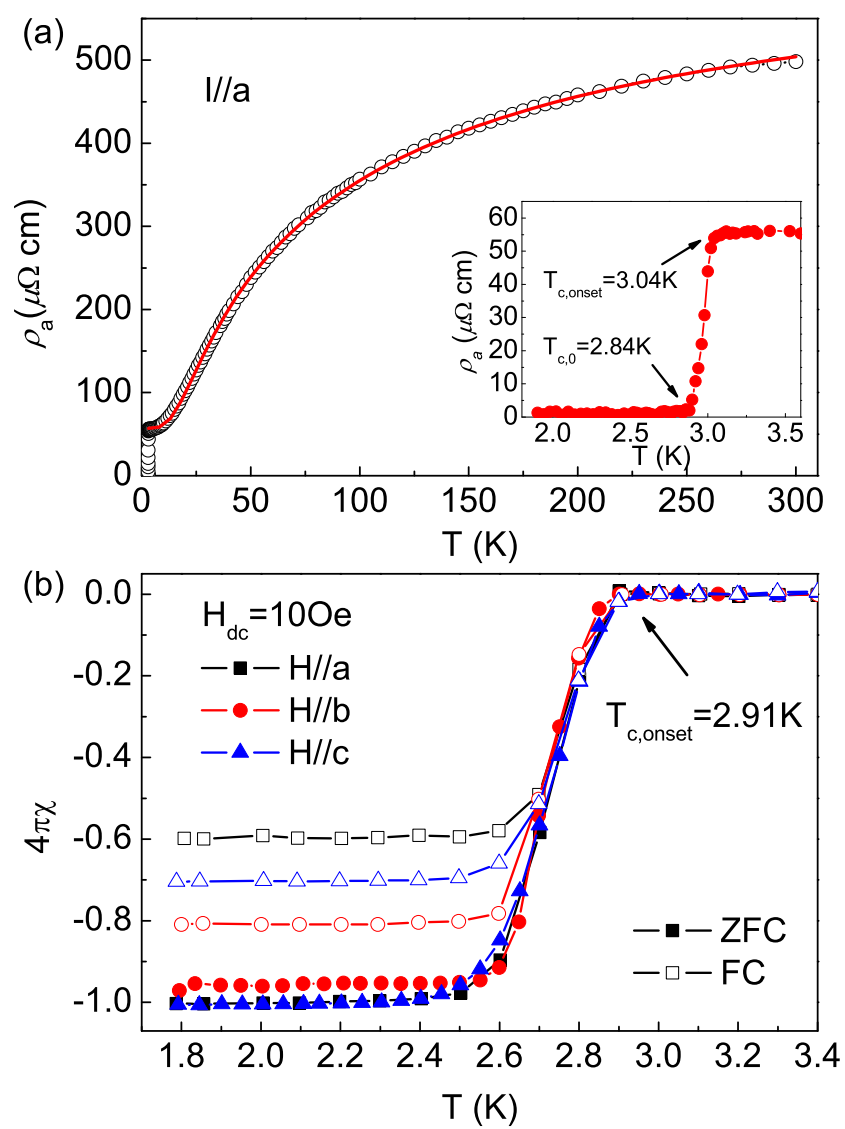


Figure 2

BR11786

16Jul2012

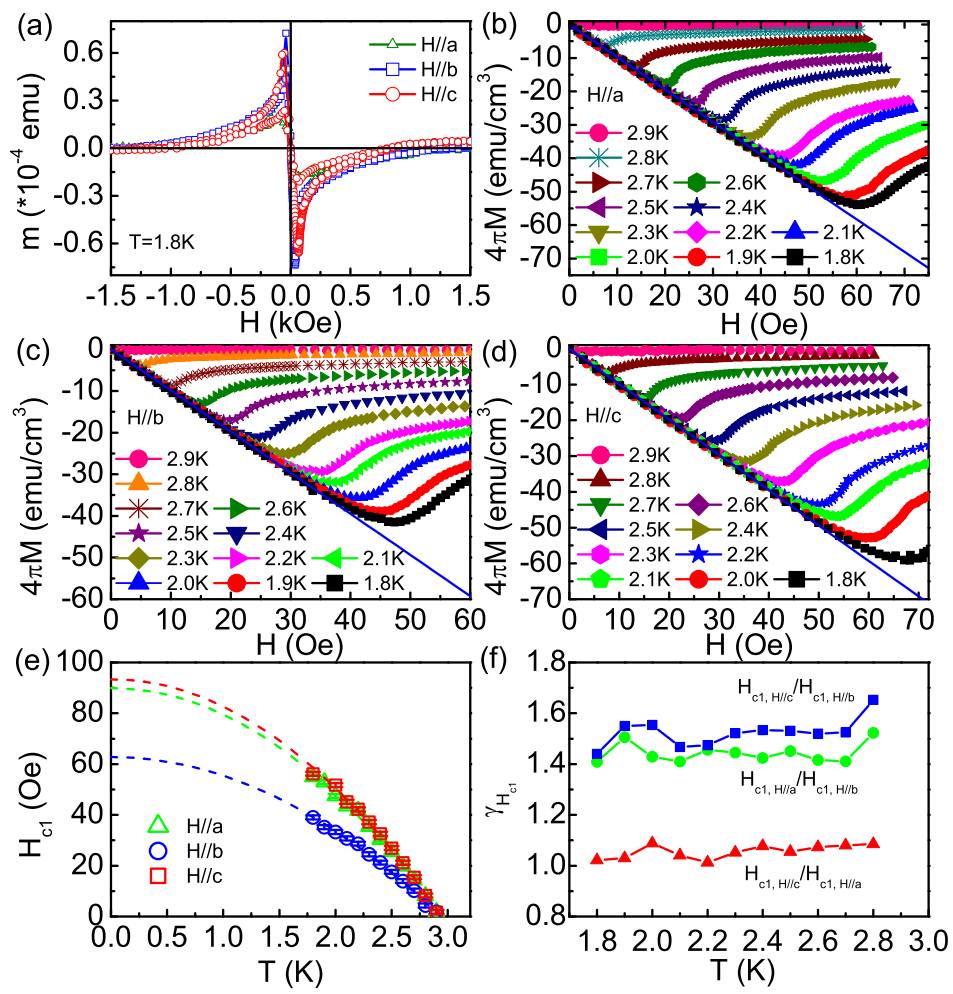


Figure 3

BR11786

16Jul2012

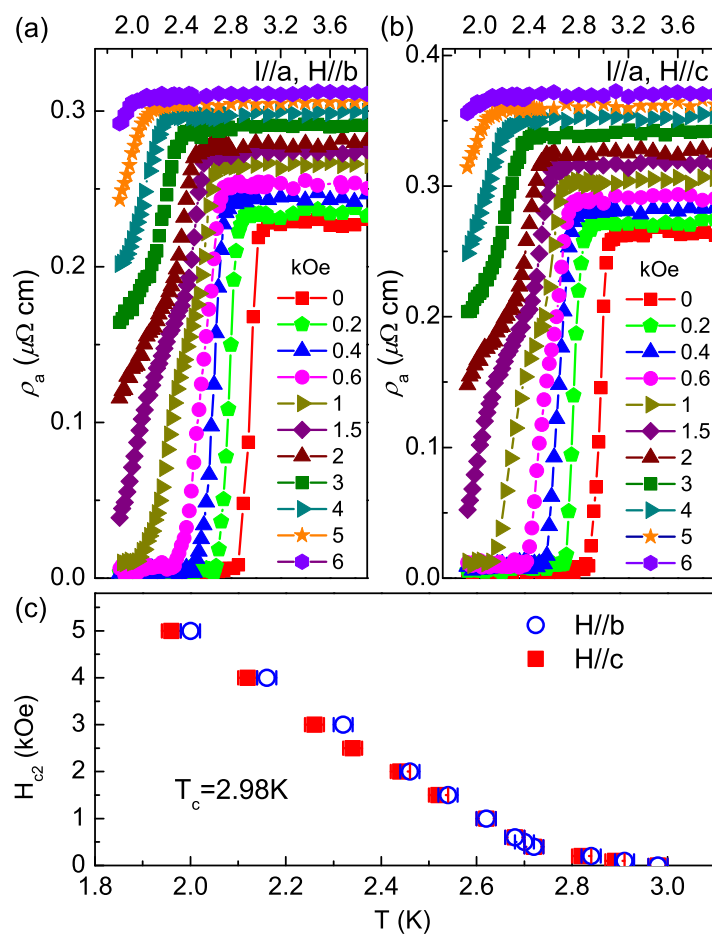


Figure 4

BR11786

16Jul2012

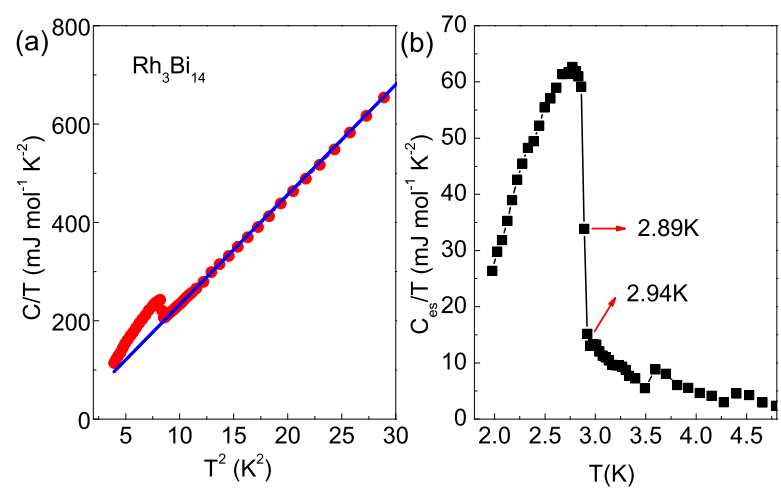


Figure 5 BR11786 16Jul2012